Math. Model. Nat. Phenom.
Vol. 3, No. 6, 2008, pp. 76-100

A Variational Framework for Assessment of the Left Ventricle Motion

J. Garcia-Barnés[a,b1], **D. Gil**[a,b], **S. Pujadas**[c], **F. Carreras**[c]

[a] Computer Science Department of Universitat Autònoma de Barcelona, Bellaterra, Spain
[b] Computer Vision Center, Bellaterra, Spain.
[c] Department of Cardiology, Cardiac Imaging Unit, Hospital Sant Pau, Barcelona, Spain

Abstract. Impairment of left ventricular contractility due to cardiovascular diseases is reflected in left ventricle (LV) motion patterns. An abnormal change of torsion or long axis shortening LV values can help with the diagnosis and follow-up of LV dysfunction. Tagged Magnetic Resonance (TMR) is a widely spread medical imaging modality that allows estimation of the myocardial tissue local deformation. In this work, we introduce a novel variational framework for extracting the left ventricle dynamics from TMR sequences. A bi-dimensional representation space of TMR images given by Gabor filter banks is defined. Tracking of the phases of the Gabor response is combined using a variational framework which regularizes the deformation field just at areas where the Gabor amplitude drops, while restoring the underlying motion otherwise. The clinical applicability of the proposed method is illustrated by extracting normality models of the ventricular torsion from 19 healthy subjects.

Key words: left ventricle dynamics, ventricular torsion, tagged magnetic resonance, motion tracking, variational framework, Gabor transform.
AMS subject classification: 35A15, 43A32

1. Introduction

Impairment of left ventricular (LV) contractility due to cardiovascular diseases is reflected in LV motion patterns, resulting from the peculiar helical disposition of LV myocardial fibers.

---

[1] Corresponding author. Email: jaumegb@cvc.uab.es

Article available at http://www.mmnp-journal.org or http://dx.doi.org/10.1051/mmnp:2008082

The detection of an abnormal change of torsion and long axis shortening LV values can help with the diagnosis and follow-up of LV dysfunction, as it occurs in pathologic conditions such as ischemic heart disease or cardiomyopathies. To this aim, a complete analysis of the global [21, 33] and also regional [6, 15, 16] function of the heart should be performed. Currently, there are many imaging techniques allowing the visualization of cardiac function. Among them, Tagged MRI [3, 35] is the reference imaging modality for regional assessment of the heart function. This technique produces a grid like pattern of saturated magnetization over the myocardium (see images in fig.1 b)). The grid deformation along the cardiac cycle allows visualization of intramural deformation and, thus, assessment of in-heart local functionality.

Since the appearance of Tagged MRI, in the late 80's, many image processing techniques have been developed in order to extract data motion. We might differentiate between those working in the image spatial domain and those working in its frequency (Fourier) domain.

In the first group [34, 20, 17] the dark stripes are considered as target features to be tracked along the sequence. A main problem is that contrast between tissue and tags diminishes in time (fading effect [25]), which lows their performance at advance stages of the cardiac cycle. Furthermore these techniques lead to sparse displacement fields that have to be further interpolated to the whole myocardium. These drawbacks can be overcome by means of a variational approach modelling brightness variation. The most popular trends are optical flow techniques [10, 11, 26] for tracking motion between consecutive frames and non-rigid registration [8, 22, 27] to the initial frame. Although they provide motion fields defined on the whole image, compensating the fading effect [17] leads to complicated numeric schemes prone to reduce computational efficiency.

In the second group we have the spectral methods which use frequency content of the tagged sequences to estimate motion. The most representative method in this group is the HARmonic Phase (HARP) [24, 25], which tracks the phase of the Fourier coefficients associated to the tagged pattern. Although such methods allow tracking motion at any time of the cardiac cycle they have two main limitations. On one hand, since they use a global Fourier transform they can not properly deal with inhomogeneous deformations usual at advanced stages of the systolic cycle (see basal and apical sequences in the first and third rows of fig. 1 b)). On the other hand, there is not any continuity constrain on the vector field which might lead to discontinuous fields at end-systole. In [2] properly modelling tissue local deformation is addressed by using a bank of Gabor filters, but still no continuity on the vector field is forced.

In this paper, we provide a novel variational approach to computation of the left ventricle dynamics observed in tagged sequences. Firstly, we introduce a bi-dimensional representation space for tagged images given by a pair of Gabor filter banks. The phase of the Gabor responses is a property of tissue that remains constant along the cardiac cycle [24] and is able to detect local deformations [4]. Meanwhile, the amplitude of the Gabor response indicates the reliability of the local pattern detected by the Gabor filter. Secondly, we define a functional in a Sobolev space [12] for tracking each of the representation features. We combine the optical flow [19] of the two Gabor phases into a variational framework which regularizes the deformation field just at areas where the Gabor amplitude drops [14]. The

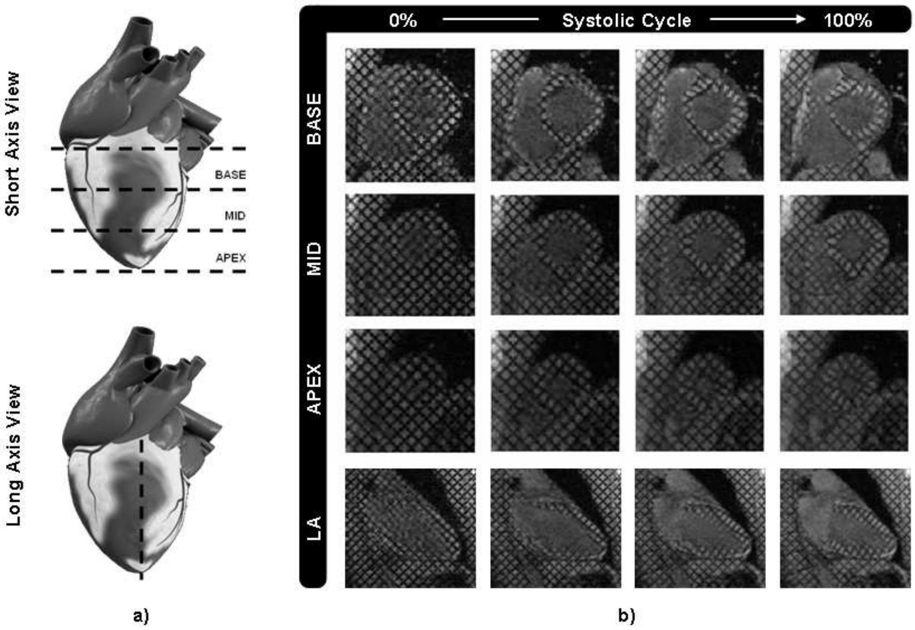

Figure 1: TMR sequences acquisition. The main LV views are shown in a), short axis (SA) above and long axis (LA) below. The SA view comprises 3 levels called Base, Mid and Apex. Sequences from each of the cuts are shown in b).

resulting deformation map is a dense and continuous vector field which we call Harmonic Phase Flow (HPF). The method accuracy has been tested using, both, synthetic dynamic phantoms and real sequences manually marked by an expert. Its clinical potential is illustrated by computing normality profiles for the ventricular rotation and torsion [23], which are strongly related to the ventricular ejection and filling [18].

The paper contents are distributed as follows. In Section 2. we detail the image processing background for motion tracking in tagged MR images. Section 3. explains our variational approach to computation of the LV motion observed in tagged MR sequences. Validation of the variational model in synthetic phantoms is detailed in Section 4., while the validation in real sequences is given in Section 5.. Its clinical applicability, including healthy normality models for the ventricular torsion, is also given in Section 5.. Finally, discussion and further lines of research are exposed in Section 6..

2. Image Processing Background

2.1. HARP Representation

An image sequence might be regarded as a uniparametric family, namely $I(x, y; t)$, of 2D functions (images or frames) indexed by the temporal variable t. The SPAMM tagging protocol [3] "prints" over the myocardium two sets of linearly independent tags generated by two main frequencies, (ω_1, ω_2), that produce K spectral harmonic peaks in the frequency domain. The number of harmonic peaks depends on the number of hard radio frequency pulses applied to produce the pattern [25]. It follows that any tagged frame $I(x, y; t)$ might be expressed [25] as the composition of complex images called *harmonic images*:

$$I(x, y; t) = \sum_{k=1}^{K} I_0(p(x, y; t)) c_k(t) e^{i\langle \omega_k, p(x,y;t)\rangle} = \sum_{k=1}^{K} I_k(x, y; t) \tag{2.1}$$

for $\omega_k = n_k\omega_1 + m_k\omega_2$; $p(x, y; t)$ the reference map that relates a spatial point (x, y) at a given time t to its associated material point at time $t = 0$; $\langle \cdot, \cdot \rangle$ the scalar product; I_0 the underlying ordinary MR image (without tags) and c_k a function modelling tags fading across time.

The phase of each *harmonic image* $\Phi_k(x, y; t) = \langle \omega_k, p(x, y; t)\rangle$, is a stable property of the tissue, as it linearly depends on the reference map [25]. Since, in practice, the phase cannot be properly retrieved, the principal wrapped value [25, 28] defined in the range $[-\pi, \pi)$ is used. This is called HARP image and it provides motion information in a direction close to ω_k. In order to extract 2D motion, two HARP images associated to linearly independent harmonic frequencies are required.

In the case of the HARP method proposed in [24], they use a Newton-Raphson approach for seeking the points that keep constant phase values between consecutive HARP images. Since the correspondence is computed separately for each pixel, the resulting vector field is often irregular.

2.2. Tracking Issues

In image processing terms, tracking [19, 5] addresses finding the trajectory of a given object in an image sequence. In a mathematical framework, object tracking turns into determining, for each time t, the map that best matches two consecutive frames. Since we have a different transformation for each couple of images (i.e. times), we have a family of maps indexed by time. We will note such maps by $T(x, y, t)$.

One of the most popular approaches for motion tracking is the Optical Flow [19]. Such technique relies on the assumption that the intensity of image structures keeps approximately constant, so that the transformation map must satisfy:

$$I(T(x, y, t); t) = const \tag{2.2}$$

By differentiating the first term with respect to time we obtain the *optical flow constraint equation*:

$$\langle \nabla I, T_t \rangle + I_t = 0 \tag{2.3}$$

where $\nabla I = (I_x, I_y)$ stands for the image gradient and I_t, T_t for the partial time derivative. The time derivative of the map T is a vector field $V(x, y; t) = (u(x, y; t), v(x, y; t))$ that best matches two consecutive frames. Using this notation we get the usual formulation for the *constrain equation*:

$$\langle \nabla I, V \rangle + I_t = 0 \tag{2.4}$$

We note that, from a mathematical point of view and under the brightness constancy assumption, object tracking converts into finding the isosurfaces of the uni-parametric family of images, $I(x, y; t)$, defining the sequence. Since only one equation (2.4) is available, in order to uniquely determining the two unknowns (u and v) smoothness constraints are usually added.

In the case of HARP images, we have, for each time t, a couple of angular values, $a_1(x, y; t)$ and $a_2(x, y; t)$, that must be tracked [13]. Therefore the deformation field could be computed by solving independently for each point the optical flow system:

$$\langle \nabla a_k, V \rangle + a_{kt} = 0 \quad \text{for} \quad k = 1, 2 \tag{2.5}$$

We note that this would yield irregular vector fields since there is no constraint on the spatial continuity of the vector. In the following section, we use these equations in a variational framework as matching term, in order to obtain continuous deformation maps.

3. Harmonic Phase Flow

3.1. Harmonic Representation

In order to obtain the HARP images associated to a given tagged frame, its main harmonic images (I_1, $I_2 \in \mathbb{C}$) need to be determined. If tags were a regular grid, band pass Gabor filters centered at the main spectral peaks, (ω_1, ω_2), would retrieve the harmonic images. Grid regularity holds at initial time (fig. 1 b), first column) but, as the myocardial cycle evolves, tags loose their initial ideal shape (Fig. 1 b), columns 2 to 4), and the previous filter will give lower response in most of the myocardial regions. The highest response will be given, at each point, by the Gabor filter with the most similar frequency and scale of the underlying tag pattern. A Gabor filter is the product of a complex sinusoid, that determines the frequency, by a gaussian envelope that determines the scale.

$$\Gamma(x, y) = C \quad \underbrace{e^{-i2\pi(\frac{\omega_x x}{W} + \frac{\omega_y y}{H})}}_{Frequency} \quad \cdot \quad \underbrace{e^{-\frac{(x')^2 + (\lambda y')^2}{2\sigma_{x'}^2}}}_{Scale} \tag{3.6}$$

Each part of the Gabor filter formula has its own parameters that can be independently tuned:

Frequency Parameters:

- $\omega = (\omega_x, \omega_y)$ is a 2D vector that determines the frequency and the orientation of the pattern with its norm and angle respectively.

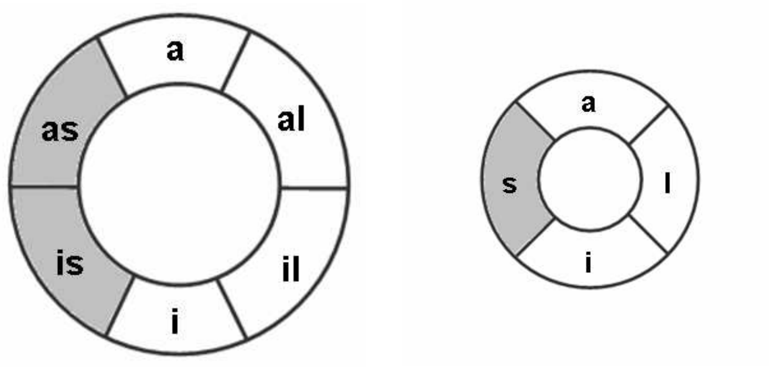

a) b)

Figure 2: American Heart Association nomenclature for myocardial segments in SA views seen from apex to base. a) Basal and mid sectors: anterior (a), anterolateral (al), inferolateral (il), inferior (i) inferoseptal (is) and anteroseptal (as). b) Apical sectors: anterior (a), lateral (l), inferior (i) and septal (s).

- H and W determines the height and the width of the window in which we define the filter. These parameters are fixed and have the same values as the image to be filtered.

Scale Parameters:

- $x' = x\cos\phi + y\sin\phi$ and $y' = -x\sin\phi + y\cos\phi$ define the rotation of the Gaussian envelope.
- $\sigma_{x'}$ determines the size of the gaussian envelope along its x' direction.
- λ defines the degree of anisotropy of the gaussian envelope.

We design two Gabor filter banks, one for each tagging direction given by ω_k's, tuned to isolate the I_k's. We note that, since tissue local deformation is not large, the frequencies of the Gabor filters should be close to the main frequencies. If we write each principal frequency in polar coordinates, $\omega_k = r_k e^{-i\theta_k}$, then nearby frequencies are given by:

$$\omega = (r_k + \triangle r)e^{-i(\theta_k + \triangle\theta)} \tag{3.7}$$

We define the new parameters $\hat{r}_k = r_k + \triangle r$ and $\hat{\theta}_k = \theta + \triangle\theta$. Regarding to scale aspects, we consider $\sigma_{x'}$ to be Q times the period of the frequency. With these redefinitions we obtain a Gabor filter bank governed by 5 parameters. We denote a parameter configuration by $\rho = (\hat{r}_k, \hat{\theta}_k \mid \phi, Q, \lambda)$ and the 5 dimensional domain where ρ takes values by $\mathcal{P}$.

We recall that image sequences come from 4 different standard acquisition planes, which can be divided in short axis (SA) and long axis (LA) views (fig. 1 a)). In addition, the SA view comprises 3 levels along the heart long axis namely: Base, Mid and Apex (fig. 1 a), above). The heart muscle anatomy [30] strongly influences the motion that the myocardium undergoes in those different views/levels (fig. 1). Following the AHA nomenclature for myocardial segments [7] (see fig. 2) the following behavior for the different sequences (seen from apex to base) along the systolic cycle can be observed:

- **Base:** All segments less anterior and anterolateral (fig. 2 a)), that undergo radial shortening, rotate counterclockwise at the beginning of the systolic cycle. They rapidly (at 15% of systole approx.) turn to clockwise rotation together to the rest of the segments until the end of the systolic cycle (see fig. 1 b), first row).
- **Mid:** Is the most simple as it mainly presents isotropic radial shortening with few rotation depending on if the acquisition plane approaches to the base or to the apex (see fig. 1 b), second row).
- **Apex:** Presents a counterclockwise rotation together to a contractile component almost homogeneous for all the LV less the inferior sector (fig. 2 b)) in which shortening is stronger (see fig. 1 b), third row).
- **Long Axis:** The most basal levels present the highest longitudinal shortening which gradually diminish as they approach to apex, which remains almost still during the whole cardiac cycle. By the other hand LV thicken as they approach to apex (see fig. 1 b), fourth row).

These observations have motivated to design a tailored bank of filters for each of the 4 kinds of sequences. Each filter bank is characterized by its parameter domain that we denote by $\mathcal{P}_k^{LA}$, $\mathcal{P}_k^{B}$, $\mathcal{P}_k^{M}$ and $\mathcal{P}_k^{A}$, with $k = \{1, 2\}$. Parameter values for each domain are specified in table 1. Value ranges are given using the notation for vector definition of MATLAB: $(a : h : b)$.

Let I_k, $k = \{1, 2\}$ be the couple of harmonic images associated a tagged image belonging to a certain acquisition plane $l \in \{B, M, A, LA\}$. We obtain them by assigning to each pixel, the maximum response of the bank of filters:

$$I_k(x, y; t) = I(x, y; t) * \Gamma_{\hat{\rho}} \qquad \hat{\rho} = max_{\rho \in \mathcal{P}_k^l} |I(x, y; t) * \Gamma_\rho| \tag{3.8}$$

This convolution (filtering) has been implemented in the Fourier space were this operation becomes a simple product as stated by the convolution theorem.

The respective phases of I_k, Φ_k, define a bivariate harmonic representation, of the tagged MR image I. On the other hand, their amplitudes $|I_k|$ indicate the reliability of the local pattern detected by the Gabor filters, in the sense that low values correspond to noise. Amplitudes serve to integrate the two phases in a variational framework [14] which regularizes the deformation field just at areas where the amplitude drops while restoring the underlying motion otherwise.

Table 1: Parameter ranges of the Gabor filter banks for each type of sequence

	$\hat{r}_k$	$\hat{\theta}_k$	ϕ	Q	λ
$\mathcal{P}_k^B$	$(\frac{r_k}{2} : \frac{r_k}{6} : 2r_k)$	$(\frac{\theta_k-\pi}{36} : \frac{\pi}{72} : \frac{\theta_k+\pi}{36})$	$(\frac{-\pi}{18} : \frac{\pi}{18} : \frac{\pi}{18})$	$(2,3)$	$(1,2)$
$\mathcal{P}_k^M$	$(\frac{r_k}{2} : \frac{r_k}{6} : \frac{3r_k}{2})$	$(\frac{\theta_k-\pi}{90} : \frac{\pi}{90} : \frac{\theta_k+\pi}{90})$	$(\frac{-\pi}{18} : \frac{\pi}{36} : \frac{\pi}{18})$	(3)	(1)
$\mathcal{P}_k^A$	$(\frac{r_k}{2} : \frac{r_k}{28} : \frac{3r_k}{2})$	$(\frac{\theta_k-\pi}{18} : \frac{\pi}{126} : \frac{\theta_k+\pi}{18})$	$(\frac{-\pi}{18} : \frac{\pi}{36} : \frac{\pi}{18})$	(3)	(1)
$\mathcal{P}_k^{LA}$	$(\frac{r_k}{2} : \frac{r_k}{6} : \frac{3r_k}{2})$	$(\frac{\theta_k-\pi}{30} : \frac{\pi}{30} : \frac{\theta_k+\pi}{30})$	$(\frac{-\pi}{18} : \frac{\pi}{36} : \frac{\pi}{18})$	(3)	(1)

3.2. Harmonic Phase Flow Approach to LV Dynamics

The LV motion between two consecutive sequence times, t and $t+1$, is given by the 2D vector field (or deformation map), $V(X) = (u(X), v(X))$ for $X = (x, y)$, best matching their bivariate harmonic representations. In variational terms, this reduces to finding the minimum of the following energy functional:

$$\varepsilon \;=\; \underbrace{\sum_{k=1}^{2} \int \|\Phi_k^{t+1}(X) - \Phi_k^t(X+V)\|^2}_{\text{Matching}} \;+\; \underbrace{\int \|\nabla V\|^2}_{\text{Regularity}}$$

for Φ_k^t and Φ_k^{t+1} the harmonic phases of tag images at time t and $t+1$ and the regularity term, $\|\nabla V\|^2 = \|\nabla u\|^2 + \|\nabla v\|^2$, the norm of the gradient of the vector field. In our case, since, in fact, we handle a tracking problem, we substitute the matching term by its optical flow [19] first order approximation. By forcing the optical flow condition, the two summands in the matching term convert into:

$$\begin{cases} \varepsilon_1 \equiv \Phi_{1x}u + \Phi_{1y}v + \Phi_{1t} = \nabla\Phi_1 \cdot V + \Phi_{1t} \\ \varepsilon_2 \equiv \Phi_{2x}u + \Phi_{2y}v + \Phi_{2t} = \nabla\Phi_2 \cdot V + \Phi_{2t} \end{cases}$$

for Φ_{kx}, Φ_{ky}, Φ_{kt}, the partial derivatives of the $k-th$ phase at time t. If we note by ε_{reg}^2 the regularity term, then the generic tracking energy becomes:

$$\varepsilon = \int (\varepsilon_1^2 + \varepsilon_2^2) + \int \varepsilon_{reg}^2 \tag{3.9}$$

Taking into account that the phase of a complex number is given by the imaginary part of its logarithm, the spatio-temporal derivatives of the phase can be computed without any wrapping effect as:

$$\Phi_{k\ell} = \frac{\left[Re(I_k)\frac{\partial Im(I_k)}{\partial \ell} - Im(I_k)\frac{\partial Re(I_k)}{\partial \ell}\right]}{|I_k|^2}$$

where $\ell = \{x, y, t\}$ and Re, Im stand for the real and imaginary parts of a complex number. Provided that the matching terms ε_k are fully given in terms of phase derivatives, we can use

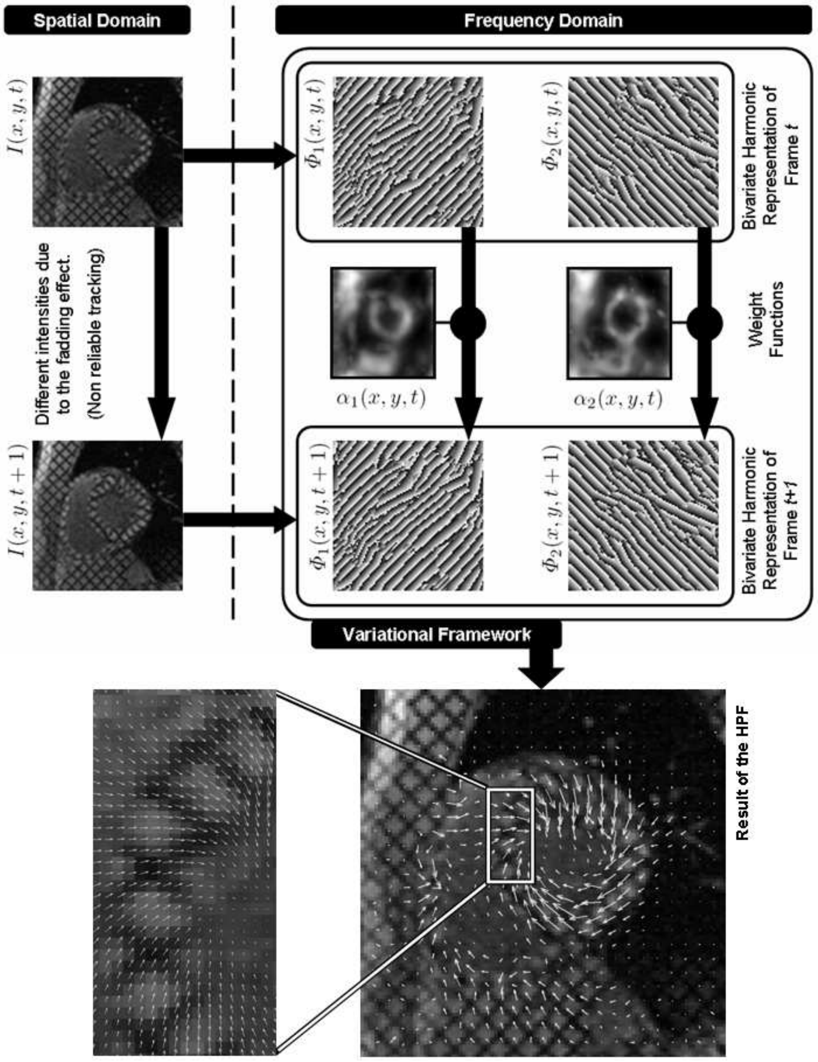

Figure 3: Main Steps in the Computation of the Left Ventricle Dynamics. Above on the left, two consecutive frames of a basal sequence. On the right their respective bi-dimensional harmonic representations that, together with the weighting functions (in the center), conform the variational framework for robust tissue tracking. Below on the right we show the result of the HPF, where vectors have been discretized and resized for visualization purposes. On the left detail of the real dense deformation map.

phases Φ_k in the tracking process even without knowing them explicitly. Recall that only their wrapped version a_k was available.

At areas with low signal to noise ratio (e.g. in the presence of thermal noise), the phases Φ_k are not reliable and, thus, should not be taken into account for motion tracking. By adding a weighting function to the energy (3.9) the latter requirement is achieved:

$$\varepsilon = \int (1 - (\alpha_1 + \alpha_2)/2)^2 \varepsilon_{reg}^2 + [\alpha_1^2 \varepsilon_1^2 + \alpha_2^2 \varepsilon_2^2] dxdy \tag{3.10}$$

where α_1 and α_2 depend on the amplitudes of I_k and are normalized in order to take values in the range $[0, 1]$:

$$\alpha_i(x, y) = \frac{|I_i|}{\|I_i\|_\infty}$$

for $\| \cdot \|_\infty$ standing for the maximum norm of a bounded function.

Since in the variational framework given by (3.10) the proposed weights depend (at each point) on the amplitude of the filtered images, the smoothness constraint is only applied at areas were the filtering response drops. Low amplitude responses correspond to myocardial areas without noticeable tagging pattern or simply background noise. In both cases, the phase does not provide any information about motion and should not be taken into account. At these areas, the vector field is linearly interpolated using the nearest reliable values. Meanwhile at clearly tagged zones, the smoothing term vanishes and only phase image motion accounts for the computation of HPF. It follows that cardiac motion discontinuities can be retrieved as far as they are detected by the tagging pattern.

We note that the proposed regularity term extends, in some sense, the formulation reported in [9]. Regularity constrains of the type suggested in [9] preserve sharp changes provided that we have an image map measuring the probability of having a meaningful discontinuity. Such map is usually defined in terms of the gradient magnitude of the target function/vector field. In the case of deformation maps in biomedical imaging, a large gradient might possibly be product of a noisy match and, thus, alternate measures are required. Modifying the metric for the L^2 regularity term is the easiest way of obtaining a weighted Laplacian (like in [9]) ensuring special treatment of singularities in the case that they are not defined in terms of the unknown input. We conclude that the proposed scheme generalizes the ideas reported in [9] without increasing the complexity of the numeric scheme (no hyper-parameter extra minimization is required) and providing a good robustness to noise.

Applying the Euler-Lagrange equations to (3.10), we get:

$$\begin{aligned} [A_{11}u + A_{12}v + A_{13}] &= (1 - \alpha)^2 \Delta u - 2(1 - \alpha)(\alpha_x u_x + \alpha_y u_y) \\ [A_{21}u + A_{22}v + A_{23}] &= (1 - \alpha)^2 \Delta v - 2(1 - \alpha)(\alpha_x v_x + \alpha_y v_y) \end{aligned} \tag{3.11}$$

where $\alpha = \frac{(\alpha_1 + \alpha_2)}{2}$, Δ is the Laplacian operator and the coefficients A_{ij} are equal to:

$$\begin{aligned} A_{11} &= (\alpha_1^2 \Phi_{1x}^2 + \alpha_2^2 \Phi_{2x}^2) \\ A_{12} &= (\alpha_1^2 \Phi_{1x} \Phi_{1y} + \alpha_2^2 \Phi_{2x} \Phi_{2y}) \\ A_{13} &= (\alpha_1^2 \Phi_{1x} \Phi_{1t} + \alpha_2^2 \Phi_{2x} \Phi_{2t}) \\ A_{21} &= A_{12} \\ A_{22} &= (\alpha_1^2 \Phi_{1y}^2 + \alpha_2^2 \Phi_{2y}^2) \\ A_{23} &= (\alpha_1^2 \Phi_{1y} \Phi_{1t} + \alpha_2^2 \Phi_{2y} \Phi_{2t}) \end{aligned}$$

The solution to the system (3.11) is the deformation map that we call *Harmonic Phase Flow*.

Figure 3 sketches the main steps involved in the computation of the LV dynamics. Above on the left, we can appreciate two incoming consecutive frames of a tagged sequence for which we want to estimate the deformation among them. On the right, we show their wrapped bi-dimensional harmonic representation which is depicted via stripe-like images. Images shown in the center, that resemble the first frame without tags, are the weight functions and represent the local reliability of the harmonic representation. The phases and the weights are combined using the variational framework defined in (3.10) to obtain the dense harmonic phase flow shown below.

3.3. Numerical Issues

The solution to the HPF flow is computed using an iterative finite difference scheme. Let $g = \begin{pmatrix} \alpha_1^2 & 0 \\ 0 & \alpha_2^2 \end{pmatrix}$, $\alpha = \frac{(\alpha_1+\alpha_2)}{2}$ and $\Phi = (\Phi_1, \Phi_2)$, then the Euler-Lagrange equation (3.11) has the compact writing given by:

$$\begin{aligned} (\Phi_x g \Phi_x')u + (\Phi_x g \Phi_y')v + \Phi_x g \Phi_t' &= (1-\alpha)^2 \Delta u - 2(1-\alpha)\langle \nabla\alpha, \nabla u\rangle \\ (\Phi_x g \Phi_y')u + (\Phi_y g \Phi_y')v + \Phi_y g \Phi_t' &= (1-\alpha)^2 \Delta v - 2(1-\alpha)\langle \nabla\alpha, \nabla v\rangle \end{aligned} \tag{3.12}$$

for $\langle \cdot, \cdot \rangle$ denoting the scalar product and $'$ the transpose of a vector. The system (3.12) can be solved by treating u and v as functions of time and solving the gradient descent scheme:

$$\begin{aligned} &u_t(x,y,t) = -[(\Phi_x g \Phi_x)u(x,y,t) + (\Phi_x g \Phi_y)v(x,y,t) + \Phi_x g \Phi_t - \\ &-(1-\alpha)^2 \Delta u(x,y,t) + 2(1-\alpha)\langle \nabla\alpha, \nabla u(x,y,t)\rangle] \\ &v_t(x,y,t) = -[(\Phi_x g \Phi_y)u(x,y,t) + (\Phi_y g \Phi_y)v(x,y,t) + \Phi_y g \Phi_t - \\ &-(1-\alpha)^2 \Delta v(x,y,t) + 2(1-\alpha)\langle \nabla\alpha, \nabla v(x,y,t)\rangle] \end{aligned} \tag{3.13}$$

The steady-state of the above system of linear parabolic partial differential equations is the solution to the Euler-Lagrange problem (3.11).

The first derivatives of the equation coefficients are computed using centered derivatives. In order to set up the discrete iterative solution, let the indexes i, j and n correspond to the continuous variables x, y and t, respectively, and let the spacing between pixels be h_x and h_y and the time step h_t. Then the partial derivatives can be approximated by finite differences as:

$$\begin{aligned} &u_t = \tfrac{1}{h_t}(u_{i,j}^{n+1} - u_{i,j}^{n}) \\ &v_t = \tfrac{1}{h_t}(v_{i,j}^{n+1} - v_{i,j}^{n}) \\ &u_x = \tfrac{1}{2h_x}(u_{i,j+1} - u_{i,j-1}) \;\; u_y = \tfrac{1}{2h_y}(u_{i-1,j} - u_{i+1,j}) \\ &v_x = \tfrac{1}{2h_x}(v_{i,j+1} - v_{i,j-1}) \;\; v_y = \tfrac{1}{2h_y}(v_{i-1,j} - v_{i+1,j}) \\ &\Delta u = \tfrac{1}{h_x^2}(u_{i,j+1} - 2u_{i,j} + u_{i,j-1}) + \tfrac{1}{h_y^2}(u_{i+1,j} - 2u_{i,j} + u_{i-1,j}) \\ &\Delta v = \tfrac{1}{h_x^2}(v_{i,j+1} - 2v_{i,j} + v_{i,j-1}) + \tfrac{1}{h_y^2}(v_{i+1,j} - 2v_{i,j} + v_{i-1,j}) \end{aligned}$$

Substituting these expressions into (3.13) and assuming equal spacing for pixels, namely h, we get our iterative approach to HPF computation:

$$\begin{aligned} u_{i,j}^{n+1} &= u^n + r(u_{i+1,j}^n + u_{i,j+1}^n + u_{i-1,j}^n + u_{i,j-1}^n - 4u_{i,j}^n) - \\ &- \frac{(1-\alpha)h_t\alpha_x}{h}(u_{i,j+1}^n - u_{i,j-1}^n) - \frac{(1-\alpha)h_t\alpha_y}{h}(u_{i-1,j}^n - u_{i+1,j}^n) - \\ &- (a_{11}h_t u^n + a_{12}h_t v^n + b_1 h_t) \\ v_{i,j}^{n+1} &= v^n + r(v_{i+1,j} + v_{i,j+1} + v_{i-1,j}^n + v_{i,j-1}^n - 4v_{i,j}^n) - \\ &- \frac{h_t(1-\alpha)\alpha_x}{h}(v_{i,j+1}^n - v_{i,j-1}^n) - \frac{h_t(1-\alpha)\alpha_y}{h}(v_{i-1,j}^n - v_{i+1,j}^n) - \\ &- (a_{22}h_t v^n + a_{21}h_t u^n + b_2 h_t) \end{aligned} \tag{3.14}$$

for $a_{11} = (\Phi_x g \Phi_x)$, $a_{12} = a21 = (\Phi_x g \Phi_y)$, $a_{22} = (\Phi_y g \Phi_y)$, $b_1 = \Phi_x g \Phi_t$ and $b_2 = \Phi_y g \Phi_t$. The r coefficient is defined as the ratio:

$$r = \frac{(1-\alpha)^2 h_t}{h^2}$$

and determines the convergence of the iterative scheme [1, 32]. According to standard arguments of theory of numerical methods, since all coefficients are bounded, the scheme (3.14) converges as far as $r \leq 1/4$. Assuming unitary pixel spacing we have that:

$$r \leq \frac{h_t \max((1-\alpha)^2)}{h^2} \leq h_t \max((1-\alpha)^2)$$

Therefore the convergence condition is guaranteed provided that the time step satisfies:

$$h_t \leq \frac{1}{4\max((1-\alpha)^2)}$$

We recall that α measures the response to the Gabor filter. Therefore the scheme speed increases in the rate that the tagging pattern is well defined.

4. HPF Accuracy

In order to assess the performance of the proposed HPF, we have created a 3D dynamic model (fig. 4 a)). The geometry of the 3D model at initial time (end-diastole) is obtained by considering 2 prolate spheroids that intersect at the most apical point. Points between these two surfaces are tissue points called, at initial time, material points. Material points have been tagged using the SPAMM tagging equations given in [31]. They have been evolved according to the principal motions that the LV undergoes along the systolic cycle:

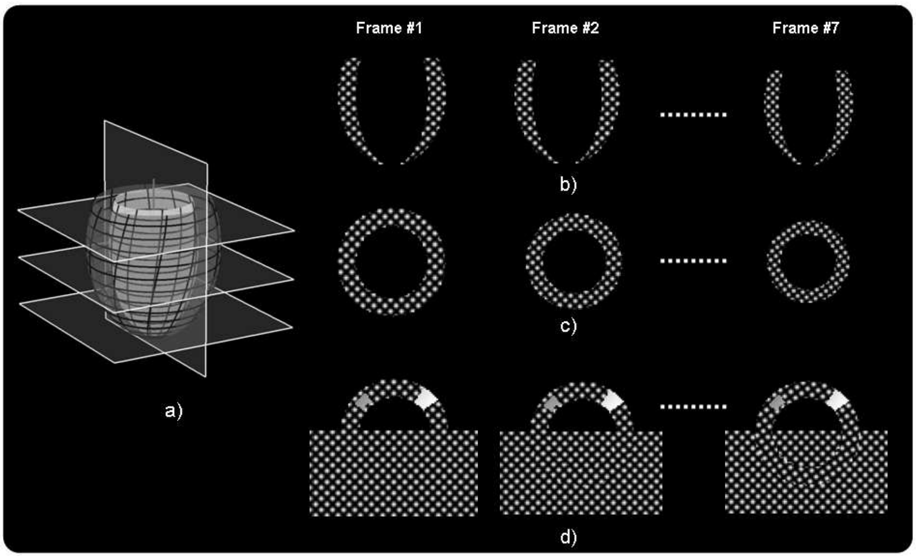

Figure 4: Dynamic Synthetic Data. a) 3D dynamic myocardial model intersected by 4 representative acquisition planes. b) Synthetic tagged frames for phantom #1 at LA and c) basal cuts. d) Basal sequence frames for phantom #2 simulating motionless (tagged and untegged) background and 2 gaps without tagging pattern.

- **Torsion:** which is the angular difference between the most basal and most apical parts of the LV.
- **Radial Shortening:** that makes the tissue to collapse towards the long axis of the LV.
- **Longitudinal Shortening:** which causes the base to contract towards the apex which, on the other hand, remains almost still.

The parameter ranges for this principal motions (obtained empirically) vary from 0 to 12 for torsion, from 0% to 18% for radial shortening and from 0% to 12% for longitudinal shortening. The model used in the present paper is composed of 7 frames corresponding to a uniform sampling of the parametric ranges. The discretization (7 frames/systolic cycle) has been chosen to produce the mean number of frames per systolic cycle we have in our experimental data. Two different 2D motion phantoms have been considered. A first phantom (phantom #1 shown in fig.4 b) and c)) is obtained by intersecting the model with planes representing the four acquisition cuts (base, middle, apex and LA). Since there is no motion information missing, phantom #1 provides the base line for any systematic errors in HPF. In order to assess HPF ability for restoring missing information and preserving discontinuities at myocardial borders, a second phantom (phantom #2, shown in fig. 4 d)) has been generated from phantom #1. Phantom #2 undergoes constant rotation and includes

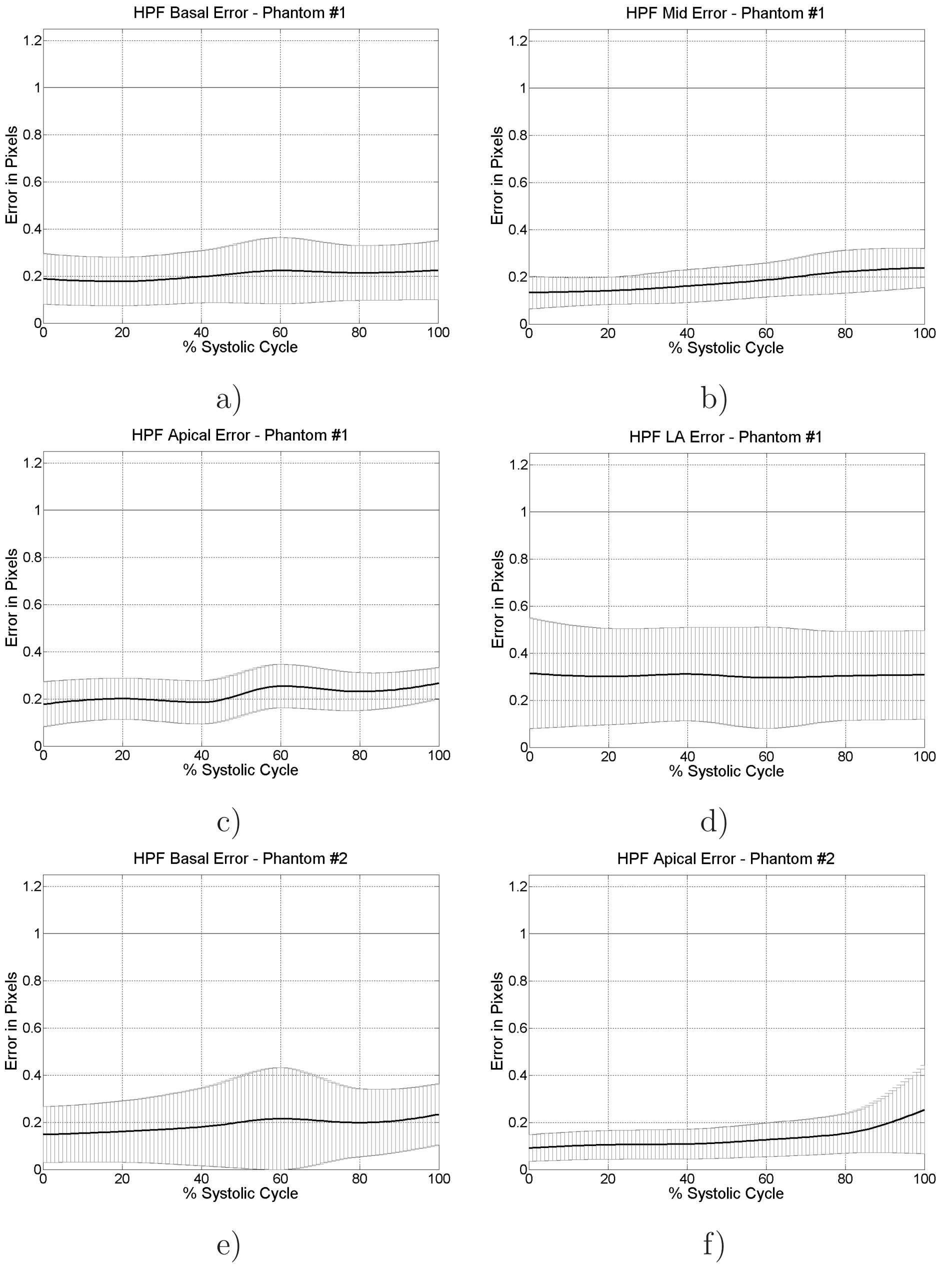

Figure 5: HPF accuracy for the 2 dynamic phantoms. In dark bold line, the mean error between the real deformation map and the estimated one along the whole systolic cycle. Vertical gray lines represent the standard deviation. Phantom #1: a) base, b) mid, c) apex and d) long axis. Phantom #2: e) base, f) apex.

surrounding still tissue, that induce discontinuities in the tagging pattern. It also includes noisy areas where the tagging pattern is not well defined or, even, missed.

The Euclidean norm of the difference between the ground truth deformation used to generate our dynamic phantom and the HPF flow is a measure of accuracy for each image pixel. The mean and standard deviation for all image pixels, provide the error range for a given frame (i.e. time). We denote by μ_l^t and σ_l^t the mean and standard deviation respectively for a given time, t, and an acquisition plane, $l \in \{B, M, A, LA\}$. The character B stands for basal cuts, M stands for mid cuts, A stands for apical cuts and LA stands for long axis cuts. The values obtained for the 7 frames of the phantom are interpolated (cubically) to the whole systolic cycle in order to provide a continuous error measure of the sequence.

Figure 5 shows the error values (in pixels) along the systolic cycle for each of the levels / views for phantom #1 (fig. 5 a)-d)), and for base and apex for phantom #2 (fig. 5 e) and f)). The dark bold line represents μ_l^t, while vertical gray lines represent σ_l^t. The errors (vertical axis) are given in pixels. Both phantoms present a similar error tendency with mean error curves (below 0.3 pixels) almost constant along the systolic cycle. In order to localize any increase in errors, their spatial distribution has been explored. Error maps along systole for the basal sequence of phantom #2 are shown in figure 6 a). Two interesting conclusions are extracted from the analysis of these error maps:

1. In general there is not any significant increase in error at myocardial boundary points with the exception of frame 4, which presents an error of 1 pixel at the lower part of the boundary. For this frame there is a sharp discrepancy between myocardial and external tagging patterns. Since the amplitude of the Gabor response depends on the strength of the main tagging pattern, at those points it has a significant decrease in α_i's values (as shown in fig.6 b)). Such decrease in the weights introduces a fake activation of the regularizing term which increases HPF error. A new measure of Gabor phase consistency is currently under development.

2. The vector field extension provided by HPF successfully restores deformation maps at gaps provided that their inner motion conforms to the motion available at their boundaries. It follows that HPF achieves a high accuracy for the empty region at the left upper part of phantom #2 in fig.4 d)). Meanwhile, in the case of the region located at the right upper part of phantom #2 the error increases due to insufficient information at its boundary.

The quality of the deformation field restored by HPF is ilustrated in fig. 7.

5. Experimental Data

Our experimental data set is composed of a total number of 19 healthy volunteers, 14 males and 5 females aged between 23 and 55 (30±7.4). For each volunteer, several (ranging from 6 to 8) short axis tagging sequences covering the LV from base to apex were acquired. Also 4 equidistributed long axis planes (including 2 and 4 chambers) were obtained. In order

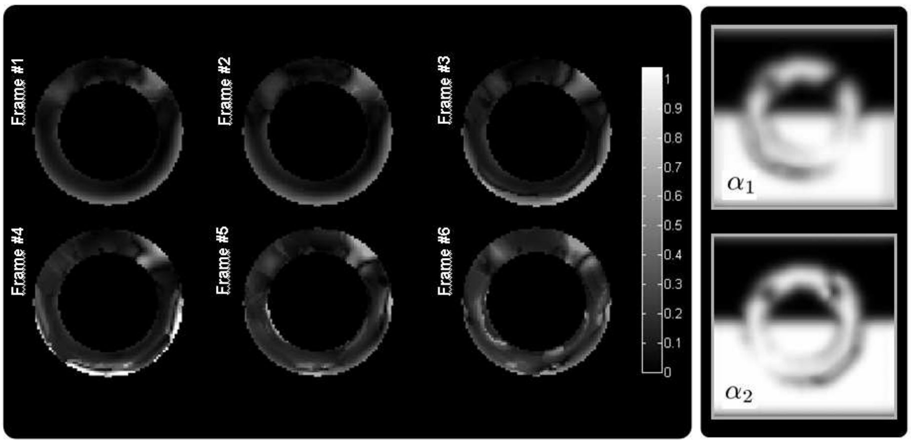

(a) (b)

Figure 6: HPF Error distribution analysis for phantom #2.: Error maps along systolic cycle in a), and image weights (α_1, α_2) of the regularization term for frame 4 in b).

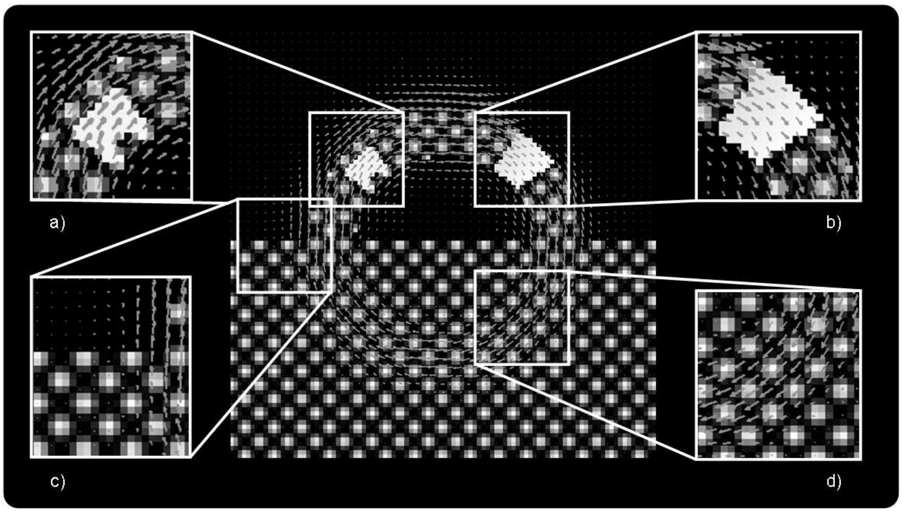

Figure 7: Details for a frame of the phantom #2 after applying HPF. In a) and b) gaps (noise) have been filled with the surrounding values, due to action of the regularizing term of the variational framework. In c) we can appreciate that in still tissue and air HPF detects no motion. In d) we can observe motion detected over the left ventricular tissue.

to avoid misalignments due to breathing, sequences were recorded in breath-hold. For the acquisition of the tagged sequences, a Siemens Avanto 1.5 T (Erlangen, Germany) equipment was used. Images have an in-plane spatial resolution of 1.3 × 1.3 mm per pixel a thickness of 6 mm per cut and a tag spacing of 4 mm. The flip angle is 14, the repetition time is 46 ms. and the echo time is 3.8 ms. Our sequences have approximately 7 frames (of mean size

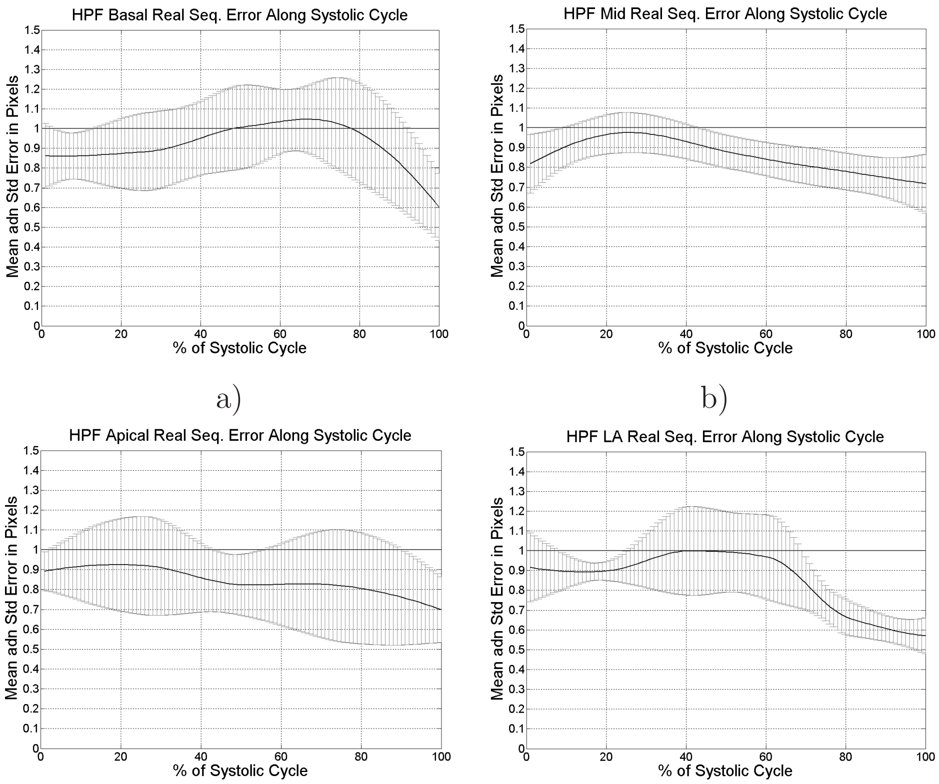

a) b) c) d)

Figure 8: HPF accuracy for experimental data. In dark bold line, the mean error between the real deformation map and the estimated one, along the whole systolic cycle. Vertical gray lines represent the standard deviation for a) base, b) mid, c) apex and d) long axis.

89 × 94 pixels) per systolic cycle.

In a standard PC(Intel® Pentium® D CPU 3.00GHz.) processing sequences using MATLAB takes about 2.6 min. for basal sequences, 0.8 min. for mid sequences, 3.1 min. for apical sequences and 2.8 min. for LA sequences. The former processing times for the computation of HPF include the two main steps: tuning of the Gabor filter banks for each view and iterative solving of equation (14). In all cases, equation (14) converges in about 125 iterations independently of the considered sequence view. The difference in times is essentially due to the filtering process. The number of filters to apply depends on the complexity of the motion observed. In this sense, since mid sequences present the simplest behavior they have a smaller bank of filters.

Table 2: Mean values of rotation and their standard deviation for basal (BR), mid (MR)and apical (AR) levels. Torsion (T) is also showed. Values are given for 6 stages of the systolic cycle: at 17%, 33%, 50%, 67%, 83%, and 100%.

	17%	33%	50%	67%	83%	100%
BR	0.7 ± 0.2	0.6 ± 0.5	-0.7 ± 0.8	-2.3 ± 1.0	-3.3 ± 1.0	-3.2 ± 1
MR	1.3 ± 0.3	2.5 ± 0.4	2.2 ± 0.7	1.5 ± 0.9	1.4 ± 0.9	2.7 ± 1.6
AR	1.5 ± 0.3	2.8 ± 0.7	3.3 ± 1	3.6 ± 1.3	4.6 ± 1.5	7.4 ± 2
T	0.7 ± 0.4	2.2 ± 0.7	4.1 ± 1	6 ± 1.4	7.8 ± 1.7	10.7 ± 1.8

5.1. Experimental Accuracy

For assessing experimental accuracy, we have analyzed 7 cases randomly selected. For each sequence, we have automatically (and randomly) selected $N(=25)$ points uniformly spread inside the LV at the initial frame. An expert was asked to manually track these points along the systolic cycle, which provided us with an "expert-dependent" sparse ground truth. For each sequence, its error has been computed as in the previous section. Precision results for each type of sequence (Basal, Mid, Apical and LA) are given by the mean and standard deviation computed over the 7 cases.

Results can be seen separately for each type of sequence in figure 8, where the mean is depicted in dark bold line and the standard deviation is represented in vertical gray lines. As in the previous section, error ranges are given in pixels. Although the error is higher than in synthetic sequences, the mean error is close to pixel accuracy. In fact, it keeps within subpixel accuracy with the exception of the basal cut between 50% and 80% of the systolic cycle. We attribute this fact to the presence of large zones with noise over the myocardium. It follows that the reliable information provided by the HARP images is so sparse that HPF restores a flow that is prone to differ from the true motion.

In figure 9 we show the HPF-based tracking of the myocardial tissue in 3 stages covering the systolic cycle. Contours have been segmented manually at the initial frame and automatically evolved in further stages.

5.2. Clinical Applicability

We have computed the normality patterns for the basal, mid and apical rotation, and the myocardial torsion. Although torsion is an oversimplified value, it is of clinical interest since it is a simple score that reflects the overall cardiac function (like the widely used ejection fraction) as it relates to the LV ejection and filling [18]. Rotational data was obtained taking as reference, points at initial time of systole (material points). The trajectory of these points was taken into account and for each one the rotation with respect its material point was computed using as center of rotation the centroid of the left ventricle at each frame. Rotation

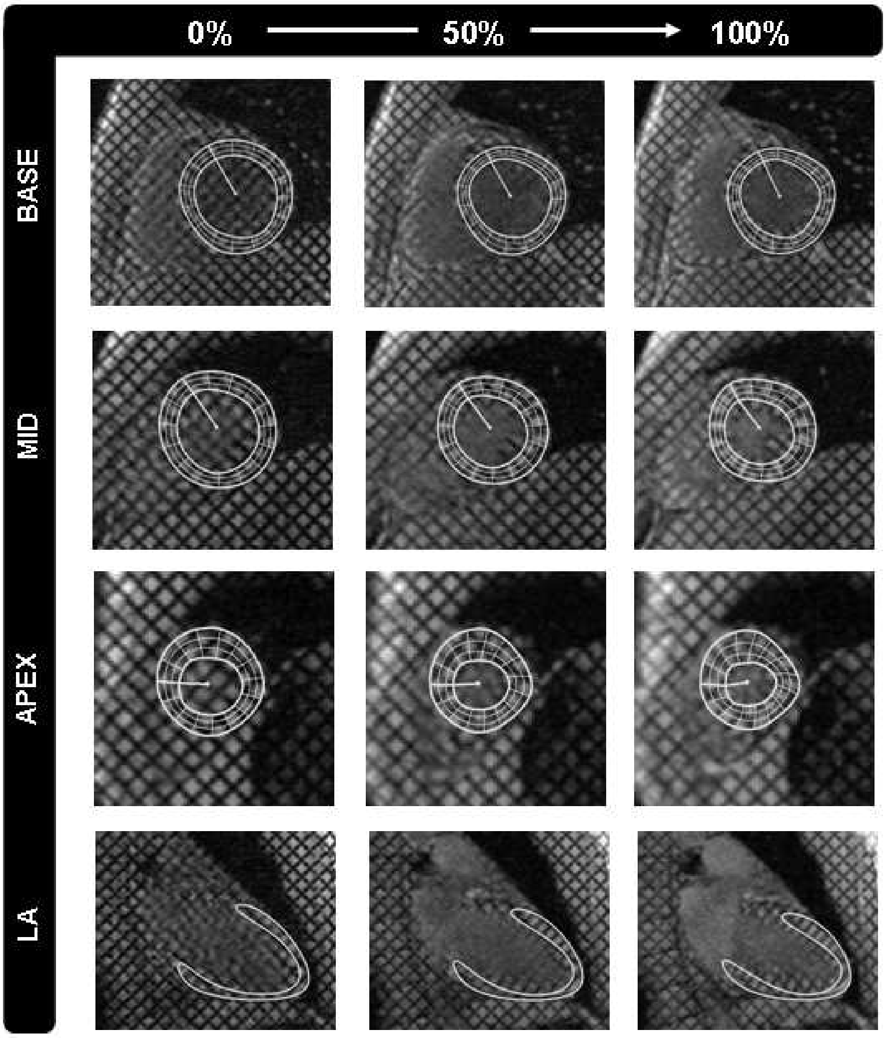

Figure 9: HPF-based contour tracking. The initial contours (first column) of basal, mid, apical and LA instances, have been tracked using HPF, and results are shown at 50% (second row) and 100% of the systolic cycle.

at a certain instant, arises as the mean rotation of all the points in the myocardium at such instant. The myocardial torsion is defined as the difference in rotation between the most apical and basal short axis planes. Normality patterns are obtained by averaging the rotation profiles extracted from the 19 healthy cases. Trimmed statistics (computed with values between the percentiles 5% and 95%) were used to minimize the impact of artifacts during acquisition time. Tagged MRI acquisition might present the following 2 artifacts: Subject motion and variability in the position of the acquisition plane. A strong presence of both phenomena might introduce outlying motions, although this seldom happens (approximately a 6% of the cases in our sequences).

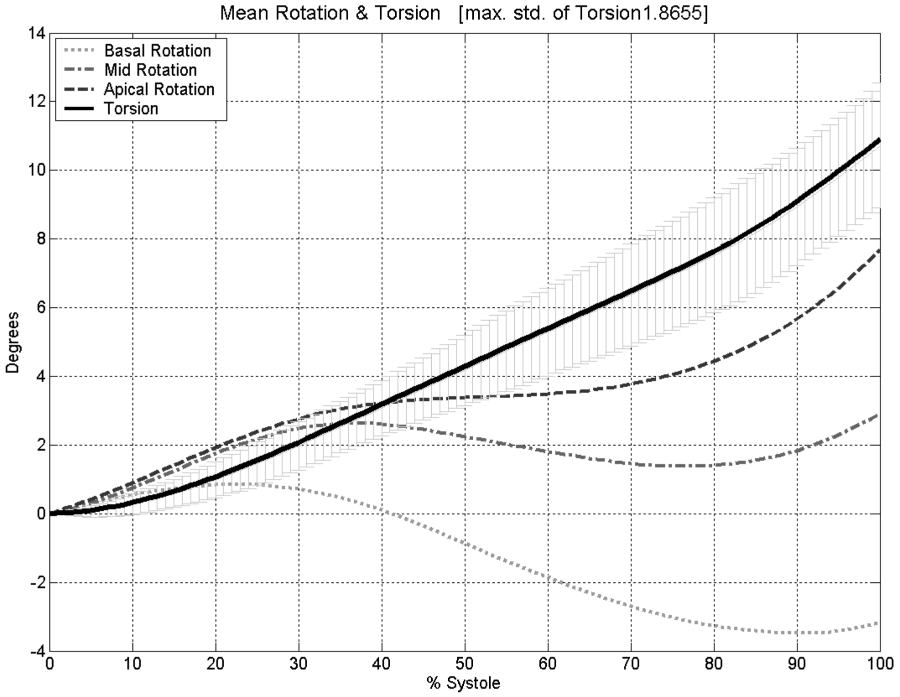

Figure 10: Normality Patterns for basal, mid and apical rotation and myocardial torsion, extracted from a set of 19 healthy volunteers. Torsional values are obtained by the difference between the apical and basal rotations.

The normality patterns for rotation and torsion are plotted in fig.10. The horizontal axis shows the percentage of the systolic cycle achieved and the vertical one the rotation and torsion in degrees. In the case of the torsion we show (in bright gray lines) its variability range given by the standard deviation of the 19 patterns considered. The average plots for rotation show that all three levels start rotating counterclockwise (seen from apex to base) and at 23% and 38% of the cycle, base and mid change to clockwise rotation respectively. At these points they reached a rotation of 0.85 and 2.63. Later, at 92% and 78% (−3.48, 1.37) base and mid, turn again to counterclockwise rotation until reaching the end of the systolic cycle (−3.2, 2.7). On the other hand, apex experiments a non-decreasing rotation (counterclockwise) during all the systolic cycle. In its central interval, from 45% to 64% approximately, rotation remains almost constant as it varies from 3.3 to 3.5. This fact means that, in this period of time, radial shortening predominates over rotation. It is worth to mention that, despite the nonlinear rotational behavior that all levels undergo, the resultant torsion values vary almost linearly with time. We note that the curves obtained with the HPF are comparable to those obtained by manually selecting points in [23].

In Table 2 we show the numeric range at some representative systolic stages. Statistical ranges are given by the mean plus minus the standard deviation of the subjects analyzed. We attribute the apparent increase in ranges for torsion to an increase in its values, since, in fact, the relative range decreases from 57% at begin systole to 16% at end-systole. Still, a standard deviation below 2 selects torsion as a reliable parameter to be taken into account in clinical routine for myocardial function assessment.

6. Discussion and Future Research

In this paper we have presented a novel method to track left ventricular deformations along the whole systolic cycle from tagged MR sequences. Gabor filter banks provide a bi-dimensional harmonic representation of each frame where the brightness constancy is fulfilled along the cycle. Both representations are tracked using optical flow in a variational framework that regularizes motion just in the presence of noise. The solution of this functional is the deformation map that estimates LV function and which we call Harmonic Phase Flow (HPF).

HPF accuracy has been tested in, both, synthetic and experimental data. We have generated 2 synthetic models. The first one (phantom #1) considers the main basic cardiac motions and serves to set HPF base-line error. The second one introduces background still tissue and gaps in tag pattern. In this way we have explored HPF capabilities for preserving discontinuities at myocardial borders as well as information filling. In all cases, HPF achieved subpixel accuracy (0.3 pixels average) along the whole cycle which shows that there are not any systematic errors. The analysis of error distribution for phantom #2 prompts 2 interesting properties. Firstly, HPF properly retrieves motion information in the presence of gaps in the tagging pattern. Secondly, HPF preserves motion discontinuities as far as tags do not present a sharp corner-like pattern. This might produce a decrease in HPF accuracy at some parts of the myocardial borders. This is common to all existing methods and, in our case, might be solved by modifying the weighting functions.

For experimental data we used a set of 7 sequences for each level and view. Myocardial points were manually tracked by an expert in order to provide the ground truth deformation to be compared to the HPF estimation of motion. We nota that, in this way, statistics do not take into account inter-observer variability. With the exception of a short interval in the basal sequences where it reaches 1.2 pixels, in all cases the mean error, although higher than in synthetic data, achieved subpixel accuracy. The increase in error in real sequences is due to thermal noise which corrupts the HARP images. Constancy in error along the systolic cycle proves the method robustness to the fading effect.

The clinical potential of HPF tracking is illustrated by computing normality patterns (given by the the mean and standard deviation for all cases) for two clinical global scores, myocardial rotation and torsion in 19 healthy cases. The mean and standard deviation for all subjects give normality patterns. The curves obtained correlate to the ones extracted by manually tracking myocardial points [23].

Our current research focus on two main issues:

- **Regional Normality Models of Motion**. The observable gross anatomy of the LV, is consequence of the particular disposition of the myocardial fibers in the 3D space [29]. This disposition strongly affects the dynamical behavior of the heart, leading to a non-isotropic motion of tissue. We are working on the definition of a normalized domain that will alow inter-patient comparison of their deformation maps, in order to characterize the regional dynamics at the different SA levels.
- **3D Dynamics**. The estimated deformation maps extracted from image sequences are, in fact, a 2D projection of the real deformation that heart undergoes in the 3D space. We are also working on extending the 2D apparent maps provided by the HPF to the whole myocardial 3D volume using the intersection of several SA and LA TMR acquisition planes.

Acknowledgements

We would like to thank Xavier Alomar from the Radiology Department of the La Creu Blanca Clinic, for providing the tagged sequences. This work was supported by the Spanish Government FIS projects PI070454, PI071188, FIS 04/2663 and CONSOLIDER-INGENIO 2010 (CSD2007-00018). The second author has been supported by The Ramón y Cajal Program.

References

[1] W.F. Ames *Numerical Methods for Partial Differential Equations.* New York Academic, (1993).

[2] L. Axel, L. Chung, T. Chen. *Tagged MRI Analaysis Using Gabor Filters.* IEEE International Symposium on Biomedical Imaging: From Nano to Macro, (2007), 684-687.

[3] L. Axel, L. Dougherty. *MR imaging of Motion With Spatial Modulation of Magnetization.* Radiology, 171 (1989), 841-845.

[4] J. Barajas, J. Garcia-Barnes, F. Carreras, S. Pujadas, P. Radeva. *Angle Images Using Gabor Filters in Cardiac Tagged MRI.* Artificial Intelligence Research and Development, 131 (2005), 107-114.

[5] J.L. Barron, D.J. Fleet, S.S. Beauchemin. *Performance of Optical Flow Techniques.* Int. Journal. Comp. Vis., (1993), 43-77.

[6] E. Castillo, J. Lima, D.A. Bluemke. *Regional Myocardial Function: Advances in MR imaging and Analysis.* Radiographics, 23 (2003), 127-140.

[7] M.D. Cerqueira *et al. Standardized Myocardial Segmentation and Nomenclature for Tomographic Imaging of the Heart.* Circulation, 105 (2002), 539-542.

[8] R. Chandrashekara, R. H. Mohiaddin, D. Rueckert. *Analysis of 3-D Myocardial Mo.tion in Tagged MR Images Using Nonrigid Image Registration* IEEE Trans. Med. Im., 23 (2004), No. 10, 1245-1250.

[9] P. Charbonnier, L. Blanc-Féraud, G. Aubert, M. Barlaud. *Deterministic edge-preserving regularization in computed imaging.* IEEE Transactions on Image Processing, 6 (1997), No. 2, 298-311.

[10] T. Denney, J. Prince .*Optimal Brightness Functions for Optical Flow Estimation of Deformable Motion.* IEEE Trans. Imag. Proc., 3 (1994), 178-191.

[11] L. Dougherty, J. Asmuth, A. Blom, L. Axel, R. Kumar. *Validation of an Optical Flow Method for Tag Displacement Estimation.* IEEE Trans. Med. Im., 8 (1999), 359-263.

[12] L.C. Evans. *Partial Differential Equations.* Berkeley Math. Lect. Notes, (1993).

[13] J. Garcia, G. Gil, J. Barajas, F. Carreras, S. Pujadas, P. Radeva. *Harmonic Phase Flow for Tissue Motion Estimation in Tagged MR Sequences.* CVC Internal Workshop, Computer Vision: Progress of Research and Development, 1 (2006), 18-23.

[14] J. Garcia, D. Gil, J. Barajas, F. Carreras, S. Pujades, P. Radeva. *Characterization of Ventricular Torsion in Healthy Subjects using Gabor filters in a variational framework.* IEEE Proceeding Computers in Cardiology, 33 (2006), 877-880.

[15] J. Garot, D.A. Bluemke, N.F. Osman, C.E. Rochitte, E.R. McVeigh, E.A. Zerhouni, J.L. Prince, J.A.C. Lima. *Fast Determination of Regional Myocardial Strain Fields from Tagged Cardiac Images Using Harmonic Phase MRI.* Circulation, 101 (2000), No. 9, 981-988.

[16] M.J. Gotte, T.Germans, I.K. Russel, J.J.M. Zwanenburg, J.T. Marcus, A.C. van Rossum, D.J. van Veldhuisen. *Myocardial Strain and Torsion Quantified by Cardiovascular Magnetic Resonance Tissue Tagging: Studies in Normal and Impaired Left Ventricular Function.* J. A. Coll. Cardiology, 48 (2006), , No. 10, 2002-2011.

[17] M. Guttman, J. Prince, E. McVeigh. *Tag and Contour Detection in Tagged MR Imagesof the Left Ventricle.* IEEE Trans. Med. Im., 13 (1989), 74-88.

[18] T. Helle-Valle, J. Crosby, T. Edvardsen, E. Lyseggen, B.H. Amundsen, B.D. Smith, H.J. Rosen, J.A.C. Lima, H. Torp, H. Ihlen, O.A. Smiseth. *New Noninvasive Method for Assessment of Left Ventricular Rotation.* Circulation, 112 (2005), 3149-3156.

[19] B.K.P. Horn, B.G. Schunck. *Determining Optical Flow.* Artificial Intelligence, 17 (1981), 185-204.

[20] S. Kumar, D. Goldgof. *Automatic tracking of SPAMM grid and the estimation of deformation parameters from cardiac MR images.* IEEE Trans. Med. Imag., 13 (1994), No. 10, 122-132.

[21] R.M Lang *et al. Recommendations for Chamber Quantification: A Report from the American Society of Echocardiographys Guidelines and Standards Committee and the Chamber Quantification Writing Group, Developed in Conjunction with the European Association of Echocardiography, a Branch of the European Society of Cardiology.* Journal of the American Society of Echocardiography, 18 (2005), No. 12, 1440-1463.

[22] M.J. Ledesma-Carbayo, A. Bajo, C. Santa Marta, E. Perez-David, M.A. Garcia-Fernandez, M. Desco, A. Santos. *Fully Automatic Cardiac Motion Estimation from TAgged MRI Using Non-Rigid Registration Techniques.* IEEE Proceeding Computers in Cardiology, 33 (2006), 305-308.

[23] C. Lorenz, J. Pastorek, J. Bundy. *Delineation of normal human left ventricular twist troughout systole by tagged cine magnetic resonance imaging.* J Cardiov. Magn. Reson., 2 (2000), No. 2, 97-108.

[24] N. F. Osman, W. S. Kerwin, E. R. McVeigh, J. L. Prince. *Cardiac Motion Tracking Using CINE Harmonic Phase (HARP) Magnetic Resonance Imaging.* Magnetic Resonance in Medicine, 42 (1999), 1048-1060.

[25] N. F. Osman, E. R. McVeigh, J. L. Prince. *Imaging Heart Motion Using Harmonic Phase MRI.* IEEE Trans. Med. Im., 19 (2000), 186-202.

[26] J. L. Prince, E. R. McVeigh. *Motion Estimation from Tagged MR Images.* IEEE Trans. Med. Im., 11 (1992), 238-249.

[27] N. Rougon, C. Petitjean, F. Preteux, P. Cluzel, P. Grenier *A non-rigid registration approach for quantifying myocardial contraction in tagged MRI using generalized information measures.* Medical Image Analysis, 9 (2005), No.4, 353-375.

[28] S.M.-H. Song, S. Napel, N.J. Pelc, G.H. Glover. *Phase unwarping of MR phase images using poisson equation.* IEEE Trans. Imag. Process., 4 (1995), 667-676.

[29] F. Torrent-Guasp, M. Ballester, G.D. Buckberg, F. Carreras, A. Flotats, I. Carrió, A. Ferreira, L.E. Samuels, J. Narula. *Spatial Orientation of the Ventricular Muscle Band: physiologic contribution and surgical implications.* J Thorac Cardiovasc. Surg., 122 (2001), 389-392.

[30] F. Torrent-Guasp, M.J. Kocica, A.F. Cornoc, M. Komedad, F. Carreras-Costa, A. Flotats, J. Cosin-Aguillarg, H. Wenh.*Towards new understanding of the heart structure and function.* Eur. J. Cardio-Thorac., 27 (2005), 191-201.

[31] E. Waks, R.L. Prince, A. Douglas. *Cardiac motion simulator for tagged MRI.* Math. Meth. Biomed. Imag. Anal., (1996), 182-191.

[32] C. Xu, J.L. Prince. *Snakes, Shapes and Gradient Vector Flow.* IEEE Trans. Imag. Proc., 7 (1998), No. 3, 359-369.

[33] G. Yip, M. Wang, Y. Zhang, J.W.H. Fung, P.Y. Ho, J.E. Sanderson. *Left ventricular long axis function in diastolic heart failure is reduced in both diastole and systole: time for a redefinition.* Heart Journal, 87 (2002), 121-125.

[34] A.A. Young, L. Axel. *Three-dimensional motion and deformation of the heart wall: Estimation with spatial modulation of magnetization- A model based approach.* Radiology, 185 (1992), No. 1, 241-247.

[35] E.A. Zerhouni, D.M. Parish, W.J. Rogers, A. Yang, E.P. Shapiro. *Human heart: tagging with MR imaging–a method for noninvasive assessment of myocardial motion.* Radiology, 169 (1988), No. 1, 59-63.